PROCEEDINGS, 49th Stanford Geothermal Workshop
Stanford University, Stanford, California, February 12-14, 2024
SGP-TR-227

Remote sensing-based identification of potential geothermal zones in the Himalaya-Karakoram Orogenic Belt, Northern Pakistan

Muhammad Anees[1, 2], Klaus Wemmer[1], Graciela Sosa[1], Alfons Van den Kerkhof[1], Bernd Leiss[1], Jonas Kley[1], Mumtaz Shah[3], Javed Akhter Qureshi[4]

[1]Geoscience Centre, Georg-August-Universität Göttingen, Germany

[2]Leibniz Institute for Applied Geophysics, Hannover, Germany

[3]Department of Earth Sciences, Quaid-i-Azam University, Islamabad, Pakistan

[4]Department of Earth Sciences, Karakoram International University, Gilgit, Pakistan

muhammad.anees@stud.uni-goettingen.de

Keywords: Remote sensing, Hydrothermal alteration, Himalaya, Karakoram, Pakistan

ABSTRACT

Hot springs in the granitoid and gneissic complexes of the Himalaya-Karakoram orogenic belt indicate subsurface geothermal potential, which could help meet energy demand in this region with topographic and climatic extremities. However, challenging terrain and limited accessibility constrain extensive ground-based exploration. We have utilized satellite remote sensing to identify potential areas of interest at a reconnaissance scale. Alteration minerals such as alunite, kaolinite, illite, chlorite, and micas, identified through principal component analysis of ASTER SWIR-bands, indicate active and fossil zones of hydrothermal activity. Lineament density, derived from SRTM data, shows high lineament zones associated with faults and granitoid outcrops. XRD analysis of altered samples collected from these areas of interest confirm weak to moderate alteration of biotite, K-feldspar, and plagioclase in the granitoids and gneisses. The alteration intensity increases in shear zones and suggests fracture-assisted fluid interaction. We conclude that the granitoids and gneisses (enriched with radiogenic elements) are subsurface reservoirs of the hot springs operated by topographic and fault-controlled groundwater systems. We recommend further detailed ground-based exploration in our identified potential zones for their geothermal assessment.

1. INTRODUCTION

The hot springs in northern Pakistan form the Himalayan Geothermal Belt's western part, extending along the Himalayas (Fig. 1; Tong & Zang, 1981). The Himalayan Orogen, due to the active collision between the Indian and Eurasian plates, has a high heat flow due to thick radiogenic crust, fast exhuming mountains, and young intrusions (Butler et al., 1997; Craw et al., 1997; Hochstein & Regenauer-Lieb, 1998; Chamberlain et al., 2002; Zaigham et al., 2009). The concentration of hydrothermal activity along tectonic sutures and intraplate thrust faults suggests that the percolating meteoric water can access this high background heat flow deep enough to reach boiling temperatures. Additionally, numerous alteration zones on the surface indicate high spatial and temporal variability of geothermal activity due to the rapidly evolving landscape in this mountainous area. These geothermal indications provide a promising potential for geothermal energy.

Geothermal resources are traditionally explored by surveying vast areas at a reconnaissance scale to identify geothermal reservoirs and then applying data from geophysical and geochemical surveys for modeling and resource estimation (Barbier, 2002; Arnórsson et al., 2006; Kana et al., 2015). The Gilgit-Baltistan region (of north Pakistan) is characterized as the terrain with one of the world's highest topographic reliefs, with high snow-covered mountains with glaciers and deep and narrow valleys. This mountainous terrain with limited accessibility makes traditional geological and geophysical exploration challenging. Additionally, the high cost and associated logistical problems limit the exploration over a large area. Due to these reasons, no detailed exploration or mapping has been conducted so far despite the enormous geothermal potential. Only a few studies have performed geothermal investigations, of which most analyzed the chemical composition of hot springs and calculated their reservoir temperatures using chemical geothermometers (Ahmad et al., 2001; 2002). With technological advancement, there is a need to apply novel methodologies to explore the geothermal resources in this region.

In recent decades, remote sensing technology has developed to a level commonly used for geoscience exploration, specifically geothermal exploration (van der Meer et al., 2012; 2014). Remote sensing data can be used to provide information on mineralogy, temperature, and deformation on a surface over a large and inaccessible area, which can help in better understanding the geothermal potential (Haselwimmer & Parkash, 2013; van der Meer et al., 2014). Lineament density extracted from remote sensing data can help identify areas with faults and fractures associated with tectonic deformation (Wajid et al., 2021). Thermal infrared (TIR) can provide synoptic coverage of surface indicators of geothermal systems. It can be helpful in mapping and quantification of surface thermal anomalies related to geothermal features like geysers, fumaroles, and hot springs (Coolbaugh et al., 2007). Moreover, near-short wave infrared remote sensing data is helpful in the identification and mapping of alteration minerals that are associated with hydrothermal processes in geothermal fields (Yang et al., 2001).

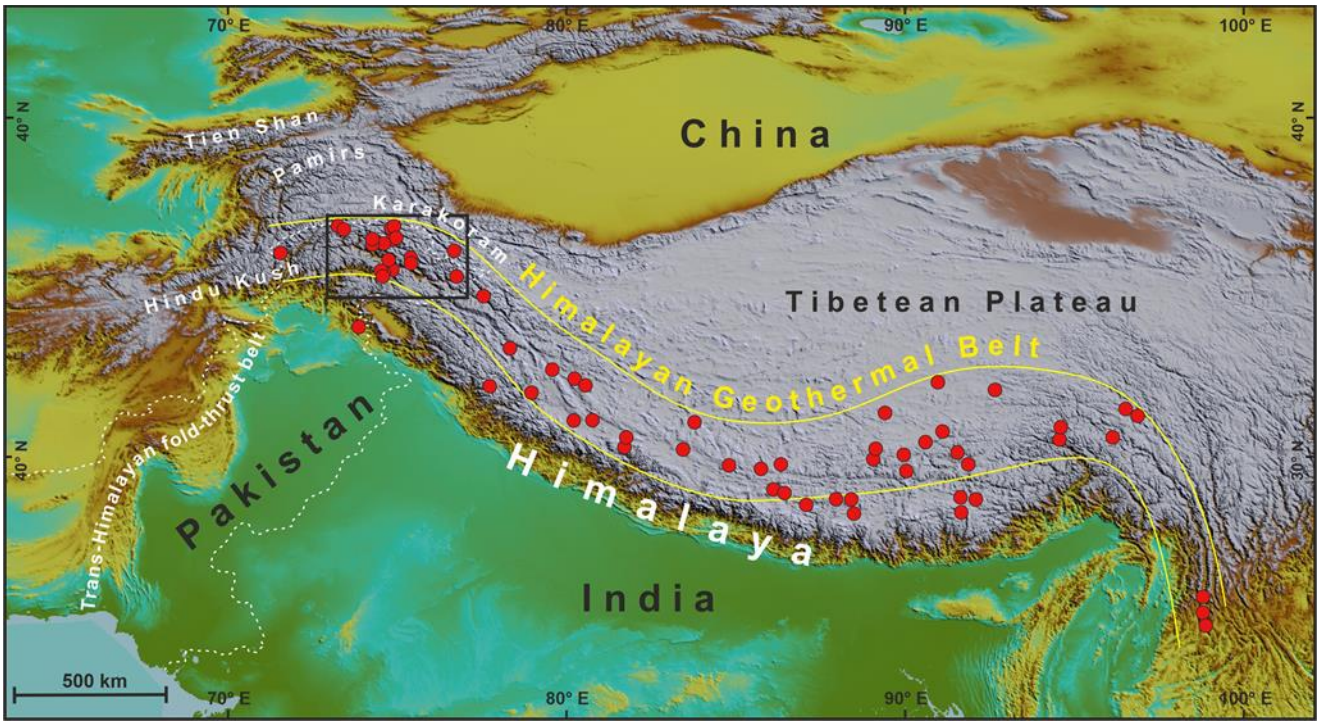

Figure 1: Topographic map of south Asia showing the distribution of hot springs of the Himalaya Geothermal Belt-HGB (after Hochstein & Zhongke, 1995) within the hinterland of India-Asia collision zone. The black rectangle shows the location of study area (in Fig. 2).

This study aims to employ remote sensing data to identify areas of interest for ground-based investigations. The identification and mapping of thermal anomalous zones has been carried out using satellite imagery. Surface lineaments and density maps have been extracted to indicate areas with high deformation. The multispectral satellite imagery was used for alteration mineral mapping to identify the areas affected by circulating hydrothermal fluids. Finally, the remote sensing results are compared with XRD analysis of samples collected from alteration zones.

2. GEOLOGICAL SETTINGS AND GEOTEHRMAL ACTIVITY

The western part of Himalayan-Karakoram orogen forms most of northern Pakistan and is tectonically subdivided from the north to the south into the Karakoram block (Asian plate), Kohistan (-Ladakh) arc, and the Indian plate (Nanga Parbat Massif) (Gaetani et al., 1996). The Kohistan arc (largely intra-oceanic) got sandwiched between Asian and Indian plates due to the closing of Neotethys along two suture zones and their subsequent collision in the Cenozoic era (Tahirkheli, 1979). These tectonic contacts are namely the Main Karakoram Thrust (MKT), which marks the boundary between the Karakoram and Kohistan, and the Main Mantle Thrust (MMT), which marks the suture between the Kohistan arc and Himalayas (Gansser, 1980; Kazmi et al., 1984).

The study area forms part of three tectonic domains, i.e., the Nanga Parbat Massif of the Himalaya, Kohistan (and Ladakh) batholith of the Kohistan (-Ladakh) arc, and Karakoram batholith of the Karakoram block (Fig. 2). The Nanga Parbat Massif (NPM) is the northernmost part of the Himalayas in Pakistan, where the Proterozoic Indian basement crust is exposed up to the elevation of ~8 km (Fig 2). The region exhibited a remarkably high uplift of up to 30 km during Himalayan orogeny (15 km in the last 3 Ma), forming an N-S striking syntaxis thrusting onto the Kohistan arc (Butler et al., 1989; Zeitler et al., 1993). It comprises Archean to mid-Proterozoic migmatitic quartzofeldspathic gneissic core, flanked by late Proterozoic calcareous and pelitic gneisses and amphibolites, with late Cenozoic pegmatitic and leucogranitic intrusions (Butler and Prior 1988; Zeitler et al., 1989). The metamorphic grade increases from amphibolite along the margins to granulite toward the massif's core.

The Kohistan-Ladakh arc is ca. 700 km long, mainly E-W trending island-arc terrane, and is sandwiched between Karakoram (of Asian plate) to the north along Shyok suture zone and the Himalaya (Indian plate) to the south along MMT. This Cretaceous intra-oceanic island arc complex has been deformed and partly metamorphosed due to its obduction onto the Indian plate to the south along MMT. The NPM's exhumation has eroded Kohistan's overlaying mass and split it into the Kohistan arc in the west and the Ladakh arc to the east (Fig. 2; Tahirkheli, 1979; Petterson, 2010). The Kohistan arc comprises a complete crustal section of the mantle to the uppermost crustal rocks. In contrast, the Ladakh arc predominantly comprises upper crustal volcanic and plutonic rocks (Treloar et al., 1990). The Kohistan batholith is formed due to magmatism (lasting ca. 86 Ma) due to the subducting Neo-Tethyan oceanic crust leading to the India-Eurasia collision (Petterson, 2010). It is a composite of gabbro-diorites, trondhjemites (Matum Das pluton), granites, and leucogranite sills and dikes (Hanzel, Jutal and Confluence granite) (Petterson et al., 1993; Treloar et al., 1996). The Ladakh batholith (the eastern equivalent of the Kohistan batholith) is predominantly composed of biotite-hornblende granites, tonalites, diorites, gabbros, and norites. It also includes volcanic units primarily exposed in its eastern parts (Singh, 1993).

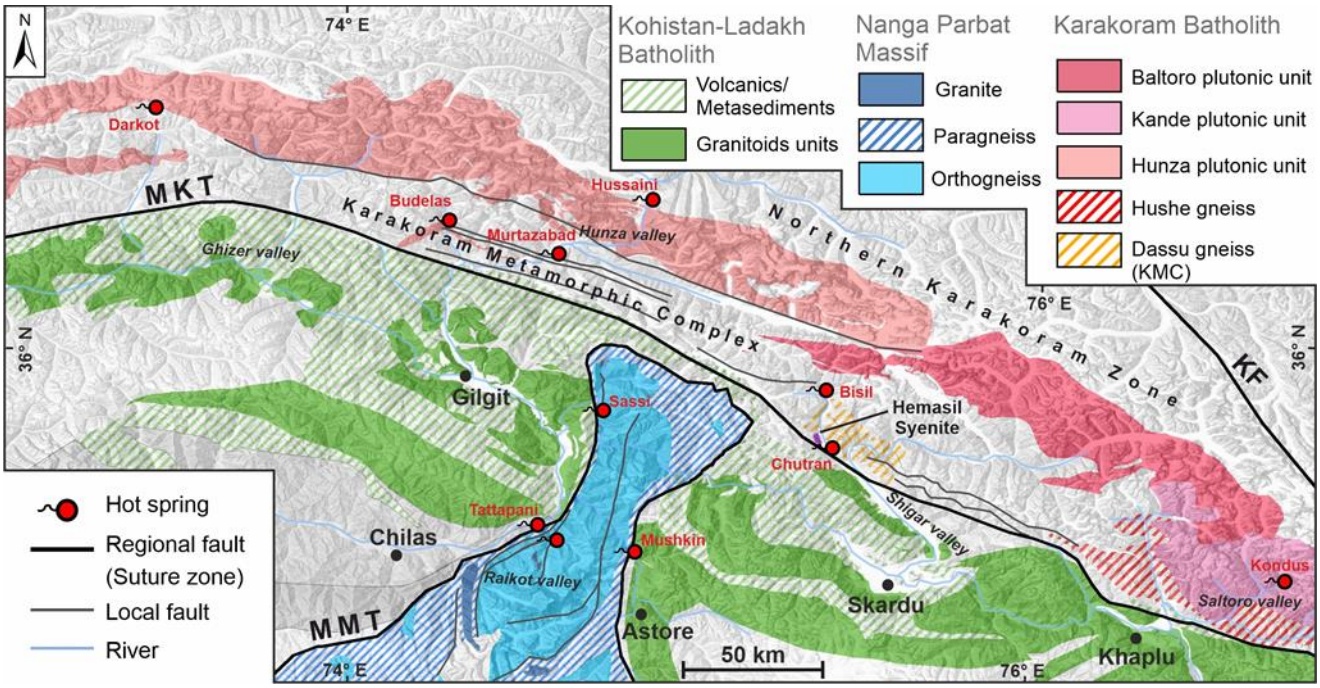

Figure 2: Geological map of the study area showing the geological units of interest (in color) and the locations of hot springs (redrawn after Madin et al., 1989; Searle & Khan, 1996; Schneider et al., 1999). Abbreviations: KF-Karakoram Fault; MKT-Main Karakoram Thrust; MMT-Main Mantle Thrust.

The Karakoram terrane represents the southern margin of the Asian plate. It is subdivided (from north to south) into the Northern Karakoram sedimentary belt, Karakoram Batholith, and Karakoram Metamorphic Complex (Searle & Khan, 1996). The northern Karakoram represents a back-arc sedimentary basin with Paleozoic carbonates and clastic sedimentary rock deposits that extend northward toward the southern Pamir (Palin et al., 2012). The Karakoram Batholith is an E-W trending, 600 km long, and up to 30 km wide axial batholith that separates the northern sedimentary sequence from the southern metamorphic complex (Searle et al., 1989; Crawford & Searle, 1992). The batholith comprises plutonic units of different ages, chemical and mineralogical composition, and tectonometamorphic history (Debon et al., 1987). It predominantly comprises Cretaceous I-type granodiorites and diorites intruded by Cenozoic leucogranites (Searle & Tirrul, 1991). The lithological units exposed in the western and central parts comprise sub-alkaline and calc-alkaline subduction-related Andean-type pre-Himalayan granitioids (Hunza plutonic unit) of mid-Cretaceous age (Crawford & Searle, 1992). The eastern part consists Jurassic diorite gneiss (Hushe gneiss) intruded by exhumation-related post-collisional leucogranites and monzogranites (Baltoro plutonic unit, Kande plutonic complex) to syenite of Miocene age (Fig. 2; Villa et al., 1996; Searle et al., 2010).

In northern Pakistan, the geothermal activity is mainly manifested as hot springs located near suture zones and active faults indicating deep fluid circulation (Fig. 2; Yousafzai et al., 2010). The hot springs in the Karakoram block mostly emerge along the MKT and associated faults. In the upper Hunza valley, the hot springs reported at Shachktar, Belli, and Hussaini, whereas towards the south, in the lower Hunza valley, several hot springs (35 - 94ºC) along with fumarole deposits are reported at Murtazabad and Hakuchar (Ahmed et al., 2002; Muhammad & Haq, 2022). Further southwest, another hot spring site is located at Budelas, where dioritic plutons intrude the metamorphic complex. Towards the east, along the MKT, hot springs emerge along the Basha River north of Shigar valley at Chutran and Bisil. In the Kondus Valley, located northeast of Saltoro Valley, hot springs emerge from fractured granite. Towards the west, along the MKT, hot springs associated with the Karakoram batholith are reported near Darkot Pass (north of Yasin Valley) and Pechus glacier (Shuja, 1986).

Along the MMT, several hot springs are present along the margins of the Nanga Parbat massif. On the eastern margin, at Mushkin, a hot spring with 57 ºC has been reported (Ahmad et al., 2002). The western margin of the massif shows higher geothermal activity with numerous hot springs at Tattapani and Sassi (Ahmad et al., 2002). This concentration of hot springs along the western margin has been attributed to the seismically active Raikot fault, which provides an escape channel for deeply infiltrated meteoric waters (Butler, 2019). Towards the core of the massif along Raikot Valley, at Tato village, a hot steaming geyser and numerous hot springs with near-boiling water (~92 ºC) are present. Besides these hot springs, alteration zones are common, indicating the interaction of meteoric water with hot rocks during exhumation and erosion (Chamberlain et al., 1995).

3. METHODOLOGY

The methodology adopted in the study is briefly explained in a flow chart in Figure 3.

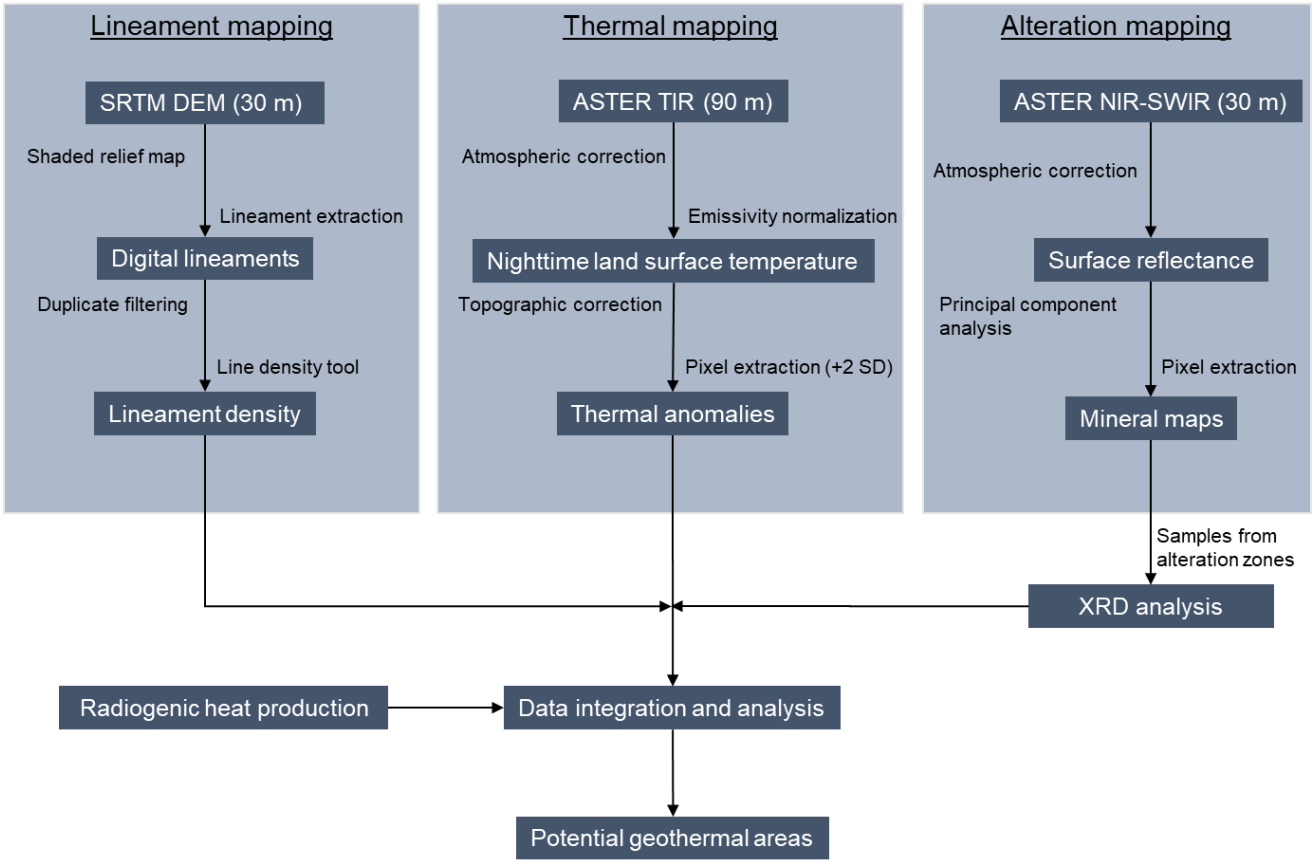

Figure 3: Flow chart of the methodology.

3.1 Lineament extraction

Lineaments are usually regarded as linear (or curvilinear) features on the earth surface which can be the expressions of geology (faults, shear zones, dykes, etc), geomorphology (valleys, rivers, ridges, etc) or other manmade (roads, canals, etc) features (O'leary at al., 1976). Satellite based topographic data has been commonly used to extract the orientations of surface landforms and interpret them as linear features (from here on termed as lineaments). In the Himalaya-Karakoram region the surface geomorphology and topography are greatly influenced by the tectonic activity and therefore, the lineaments based on geomorphological features should be in close resemblance with the surface geological features.

A semi-automated approach was to extract the lineaments using the SRTM digital elevation model (30m resolution) by shaded relief mapping through directional filtering in the ArcGIS 10.6, which sharpened the boundaries or discontinuities between the adjacent areas and helped identify lineament features such as straight valleys, straight streams segments, and rock boundaries, edges, cliffs, fault traces (Suzen & Toprak, 1998). The shaded relief map extracts lineaments based on four different azimuth angles (0°, 45°, 90°, 135°). The LINE module in PCI Geomatica was used to extract lineaments from shaded relief images obtained after directional filtering (Table 1; Thannoun, 2013). The finalized lineaments from four azimuth angles were merged in ArcGIS to generate a single vector shapefile. Postprocessing removed duplicates and redundant lineaments to obtain the final lineament data set, which was used to generate lineament density maps using ArcGIS.

Table 1: Values assigned for input parameters for extraction of lineaments in LINE module of PCI-Geomatica.

Parameter	Range	Opted value
RADI/Filter radius (pixels)	0–8192	5
GTHR/Edge gradient threshold	0–255	50
LTHR/Curve length threshold (pixels)	0–8192	10
FTHR/Line fitting error threshold (pixels)	0–8192	3
ATHR/Angular difference threshold (degrees)	0–90	15
DTHR/Linking distance threshold (pixels)	0–8192	20

3.2 ASTER Thermal data

ASTER Level-1T thermal infrared (TIR) imagery of night-time (with 90m resolution) was radiometrically and atmospherically corrected by applying respective corrections in ENVI 5.3 software. An emissivity normalization algorithm was applied to normalize emissivity values and to calculate land surface temperature (LST). Ulusoy et al. (2012) used a topographic correction to minimize the topographic effects. This correction uses statistical regression to remove the effects of elevation, aspect, and slope. Topographic correction was applied in three steps:

1. A temperature versus elevation scatter plot was used to calculate the lapse rate, which was then subtracted from the original LST image to remove the effect of elevation. 2. The elevation-corrected data was plotted against aspect data to calculate the aspect gradient, which was used to remove aspect-related errors. 3. Slope data was used to calculate and remove the slope gradient from the corrected image to obtain a final elevation, aspect, and slope corrected image.

The resultant corrected images produced thermal anomaly images in the form of positive and negative with variable magnitude from the mean.

3.3 ASTER Multispectral data

ASTER Level-1T (at sensor-radiance) multispectral imagery with three near and six shortwave infrared bands was resampled to 30 meters. The data was converted from radiance to surface reflectance using the FLAASH algorithm, which also removes the atmospheric effects from the data (Kruse, 2004). Areas with vegetation and snow were masked to exclude from the analysis. Principal component analysis (PCA) was performed to reduce the correlation among similar bands. PCA is a multivariate statistical technique that decorrelates the high-variance variables into low-variance linear principal components (Singh & Harrison, 1985).

Crosta technique was applied after Crosta et al., 2003, in which PCA was applied on four bands with reflectance and absorption specific to the target minerals, e.g., alunite, chlorite, epidote, illite, kaolinite, and sericite (or white mica). These minerals are selected as indicators of argillic (alunite and kaolinite), phyllic (illite and sericite), and prophylitic (chlorite, epidote and calcite) alterations. The resultant eigenvector matrix between the principal components (PC) indicated whether the resultant PC band corresponding to the target mineral's highest reflectance is positive or negative (Yalcin et al., 2020). If the eigenvector was positive, the target mineral was displayed in bright pixels, and if it was negative, then the dark pixels represented the target mineral (Table 2; Crosta et al., 2003).

Table 2: Eigenvector values of principal components of ASTER bands selected according to target mineral's absorption and reflection characteristics. The bold-italic values show the most decorrelated eigenvector values, based on which that specific PC band is selected for a mineral. The presented eigenvector values are for one ASTER image, which can slightly differ from another image. Carbonate (calcite) and Mg-OH (chlorite) minerals have common absorption feature and are identified as single group through ASTER data.

Mineral	Eigenvectors	Band 1	Band 3	Band 5	Band 7	Sign
Alunite	PC1	-0.50455	-0.58786	-0.44561	-0.44864	
	PC2	-0.5672	-0.32618	0.550776	0.518214	
	PC3	-0.65002	0.737508	-0.17112	-0.06538	
	PC4	0.034569	-0.06411	***-0.68469***	***0.72519***	+
Mineral	**Eigenvectors**	**Band 1**	**Band 2**	**Band 5**	**Band 8**	**Sign**
Chlorite (Calcite)	PC1	-0.56574	-0.56374	-0.45481	-0.39405	
	PC2	-0.43555	-0.41536	0.608264	0.517484	
	PC3	0.004489	-0.01076	-0.65033	0.759559	
	PC4	-0.70016	0.713831	***-0.01506***	***0.001359***	-
Mineral	**Eigenvectors**	**Band 2**	**Band 5**	**Band 8**	**Band 9**	**Sign**
Epidote	PC1	-0.52877	-0.56229	-0.48709	-0.40863	
	PC2	-0.84875	0.352571	0.299254	0.256436	
	PC3	-0.0024	-0.74713	0.475203	0.464734	
	PC4	0.003625	0.036411	***-0.66886***	***0.742484***	-
Mineral	**Eigenvectors**	**Band 1**	**Band 3**	**Band 5**	**Band 6**	**Sign**
Illite	PC1	-0.49873	-0.58244	-0.4488	-0.45892	
	PC2	-0.56465	-0.3435	0.518399	0.542623	
	PC3	-0.65757	0.736726	-0.11063	-0.11221	
	PC4	0.005365	0.002542	***-0.71945***	***0.694522***	-

Mineral	Eigenvectors	Band 1	Band 4	Band 6	Band 7	Sign
Kaolinite	PC1	-0.41742	-0.58124	-0.50127	-0.48647	
	PC2	-0.90749	0.298423	0.232811	0.18223	
	PC3	0.047067	0.566296	0.097151	-0.8171	
	PC4	0.003066	0.50241	***-0.8277***	***0.249962***	+
Mineral	Eigenvectors	Band 1	Band 6	Band 7	Band 9	Sign
Sericite (White mica)	PC1	-0.4984	-0.5536	-0.53984	-0.39205	
	PC2	-0.86652	0.338775	0.28681	0.228272	
	PC3	0.026007	0.736514	-0.65326	-0.17354	
	PC4	0.007916	-0.19055	***-0.44672***	***0.874111***	+

3.4 X-ray Diffraction

X-ray diffraction (XRD) analysis was carried out to determine semi-quantitative mineralogical analysis of the rock samples collected from the alteration zones. The bulk sample was crushed to powder (< 60 µm) using an agate ball mill. The analysis was conducted using XRD-Eigenmann's Orion Komet P2 diffractometer, equipped with a Cu anode applying 40 KV and 40 mA for measurements. The 2θ scan range was 4 to 70º and the 2θ step size 0.02º, with each step of 2 seconds. The data analysis was carried out using HighScore Plus software by Malvern Panalytical.

4. RESULTS AND DISCUSSION

4.1 Lineament mapping

A total of 12,221 lineaments covering an area of approximately 50,000 km^2 have been extracted, which were then classified into four classes according to their azimuths, i.e., N-S, NE-SW, E-W, and NW-SE. Table 3 shows the details of the distribution of classified lineaments. Of these four classes, 40 % or 4,896 are classified as E-W, followed by NE-SW lineaments amounting to 2,993 (24.5 %). Lineaments with NW-SE and N-S orientation have lower totals of 2,576 (21 %) and 1,756 (14.5 %), respectively. Similarly, out of the estimated total length of lineaments of 36,635 km, 13,935 belong to the E-W class, 9,039 belong to the NE-SW class, 7,772 belong to the NW-SE class, and 5889 belong to the N-S class.

Table 3 Azimuth-based classification of lineaments showing the number, proportion, and total length of lineaments for each respective class

Lineaments Class	Azimuths	No. of lineaments	% of lineaments	Total length of lineaments (km)
N-S	337.5 – 022.5 157.5 – 202.5	1756	14.5	5889
NE-SW	022.5 – 067.5 202.5 – 247.5	2993	24.5	9039
E-W	067.5 – 112.5 247.5 – 292.5	4896	40	13935
NW-SE	112.5 – 157.5 292.5 – 337.5	2576	21	7772
Total		12221	100	36635

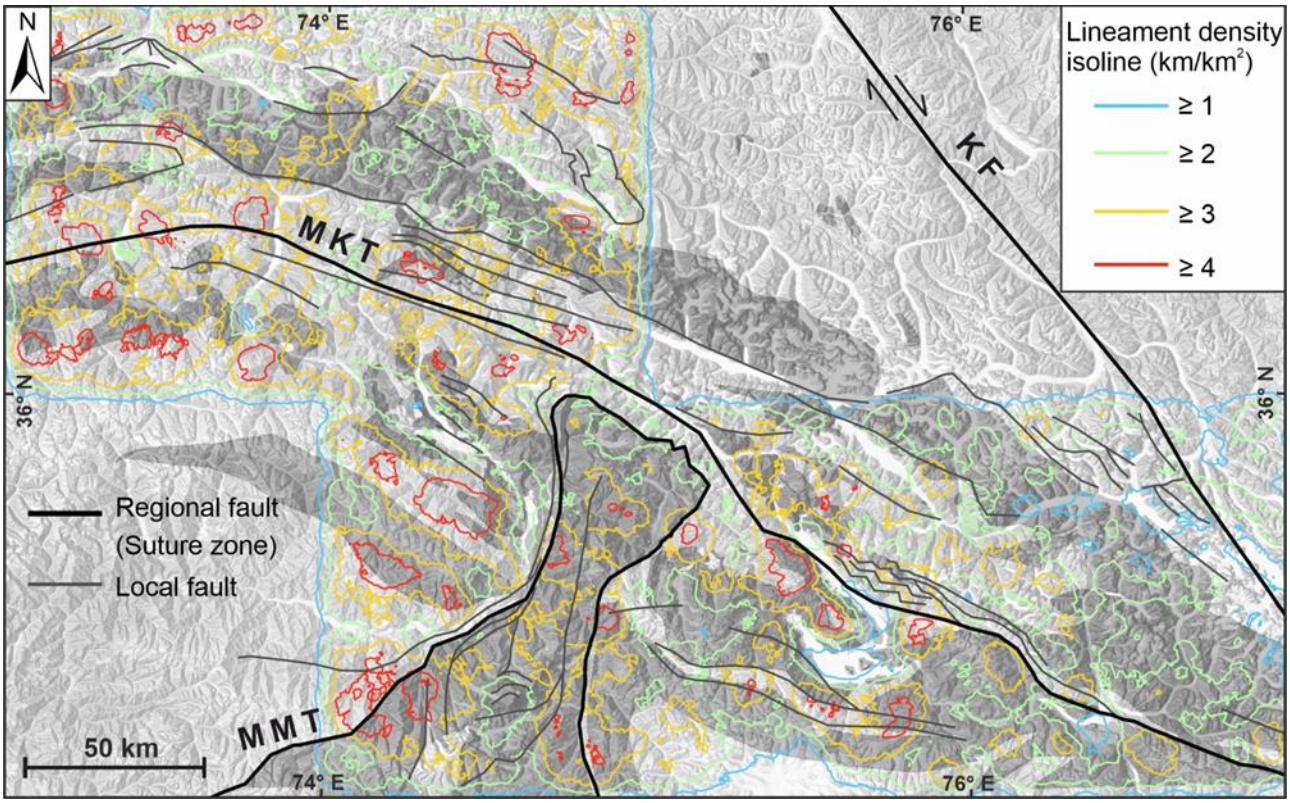

Figure 4: Lineament density map with classification into five classes (very low to very high) shows the distribution of different classes with respect to the structures in the study area. The filled grey polygons in the background indicate the lithological units of interest, i.e., granitoids and gneisses.

Figure 4 shows the lineament density map in the study area, which varies from 0 to 5.68 km/km^2 and is classified into five classes, i.e., very low (<1 km/km^2), low (1 to 2 km/km^2), moderate (2 to 3 km/km^2), high (3 to 4 km/km^2) and very high (>4 km/km^2). Glacial regions of Karakoram towards the east of the study area show low to moderate lineament density. In contrast, high lineament density is present in Kohistan and Nanga Parbat and near faults.

Structural, lithological, and topographic factors control the variations in the lineament density (Nelson, 1985). The low lineament density is found in valleys and areas covered by alluvium, while the elevated regions with exposed lithology have high lineament density. Variable lithological properties such as mineralogy, fabric, compaction, porosity, and strata thickness can induce variable degrees of jointing (Hugman & Friedman, 1979; Marshak & Mitra, 1988). However, since the area is highly deformed due to tectonic collision, the overall lineament density is attributed to the structures, where intense folding and faulting can lead to high lineament density (Barbier et al., 2012; Awdal et al., 2013). The high lineament density zones along MMT and MKT suggest that in these high-strain zones, structural control on the lineaments is dominant (Watkins et al., 2015). The absence of prominent high-density zones in the Kande plutonic complex east of the study area is attributed to topographic factors (Fig. 4), where cliffs, ice sheets, and glaciers hinder the detection of lineaments from satellite data (Ahmadi & Pekkan, 2021).

4.2 Identification of thermal anomalies

The topographic correction was applied to nighttime thermal infrared data to remove the effect of altitude, aspect, and slope. A thermal anomaly image was obtained, having positive and negative thermal anomalies around the mean value of zero. The positive thermal anomalies were further filtered by selecting the data values >1 standard deviation to show the values with the highest surface temperature compared to the surroundings. Vegetation and snow were masked to minimize the identification of false anomalies. The potential high-temperature regions lie mostly along the valleys and batholiths, but false anomalies frequently occur in the results (Fig. 5 & 6). However, despite this filter, the quality of results included high uncertainty.

The idea behind using nighttime thermal infrared data was to minimize the effect of the sun on the surface, which would help identify the areas with high background (endogenic) temperatures associated with blind geothermal activity. The initial results indicated the high influence of topography in which temperature decreased with the elevation. The topographic correction aimed to remove this effect elevation and included aspect and slope correction for differential heating from the sun during the daytime (Ulusoy et al., 2012). To this extent, the results have shown that the topographic correction has significantly decreased the topographic influence over the surface temperature. From the identified thermal anomalies, few correlated with surface lithology, hydrothermal alteration, lineament density,

and hot springs (Fig. 5 & 6). However, the distribution of most of the thermal anomalies could not be interpreted solely as a geothermal component because other environmental and physical factors can also significantly affect the temperature of a surface.

These factors include thermal inertia (dependent upon specific heat capacity and thermal conductivity), moisture content, atmospheric humidity, and differential solar heating of surfaces during daytime (Coolbaugh et al., 2007; Ramakrishnan et al., 2013). Moreover, the heterogeneous topographic shading and its variable influence on surface heating in cold and mountainous areas further increase the uncertainty (Zhang et al., 2018). Frequent or real-time ground-based monitoring of these factors, along with high temporal and spatial resolution satellite data, is required to reduce the effect of these highly variable factors. ASTER TIR product has a 90 m x 90 m pixel area and scarce data coverage in the study area, which increases the uncertainty in the results.

4.3 Hydrothermal alteration zones

Using the eigenvector matrices of PCA bands calculated separately for alunite, chlorite, epidote, illite, kaolinite, and sericite were mapped in the Shigar, Raikot, Hunza, and Saltoro valleys. An appropriate threshold was applied to each PCA band selected for the corresponding mineral in order to obtain a classified map for that specific mineral. For example, kaolinite, as an argillic alteration indicator, has absorption in ASTER bands 1 and 6 and reflection in bands 4 and 7. Therefore, PC band 4's eigenvector loading showed the most difference in bands 6 and 7, indicating that the high pixel values in PC band 4 corresponded to kaolinite (Table 2). Lineament density and thermal anomaly data are also compared to understand the correlation between these three results (Fig. 5 & 6).

The Raikot Valley shows alunite, illite, and chlorite along the Raikot fault (Fig. 5a). Kaolinite was mainly associated with leucogranite intrusions. Sericite and illite are common in orthogneiss, with scattered patches of alunite. High lineament density zones are associated with faults, and hot springs are located in these zones (Fig. 5b). However, thermal anomalies are mapped mostly over WNW-facing slopes, with one small anomaly close to a hot spring.

Epidote, sericite, and chlorite are present in the granodiorite of the Karakoram batholith (Hunza plutonic unit) in the Hunza Valley. Kaolinite is associated with mostly the granitic intrusions in the north part of the batholith (Fig. 5c). Alunite is mapped at a hot spring and several other places where dikes cross-cut the metamorphic and plutonic lithologies. Alunite, illite and epidote were mapped at Sumayar pluton. Thermal anomalies have a uniform high pattern over HPU and Sumaryar pluton (Fig 5e). However, glacial moraines are also mapped as high thermal areas. A slight correlation between lineaments and thermal anomalies is present in this area.

In Shigar Valley (Fig. 6a), alunite and muscovite are mapped close to MKT at the contact with Dassu gneiss and schist of the Karakoram metamorphic complex (KMC). Additionally, predominant alterations such as sericite, illite, and kaolinite are mapped in Dassu gneiss along the valley. Chlorite, epidote, and illite are mapped over Hemasil syenite. Alluvial fans and fluvial sediments also show deposition of alteration minerals eroded from nearby lithologies. The high lineament density areas lie near MKT, faults in KMC, and over the Shigar plutonic complex (Ladakh batholith). Thermal anomalies show a broad correlation with high lineament zones, but false anomalies are found in river sediments and some moderate lineament areas (Fig. 6b).

In Saltoro Valley, kaolinite was the most prominent alteration mineral observed associated with granitoids of Kande plutonic complex (KPC) and Hushe gneiss (Fig. 6c). Hushe gneiss, in addition to the kaolinite, also shows alteration to sericite and illite. Alunite was mapped in KPC towards the north near the hot spring. A prominent thermal anomaly was mapped in KPC along the contact with Hushe gneiss (Fig. 6d). However, the overall moderate lineament density lacked any correlation with thermal anomalies.

4.4 Alteration minerals and potential hydrothermal processes

Table 4 and Figures 5 (e & f) & 6 (e & f) show a semi-quantitative XRD analysis of the samples collected from alteration zones. RK-4alt, collected from Raikot Valley in the NPM, consists of quartz, albite, orthoclase, and biotite as major components, while chlorite, calcite, and kaolinite are alteration products. From Hunza Valley, the sample MT-1alt collected from the alteration zone near the hot spring comprises quartz, kaolinite, and alunite. SGH-1alt, collected from the alteration zone in Shigar Valley, comprises quartz, albite, and white mica (illite / muscovite) as major constituents, while jarosite and anorthoclase are minor components. Granitoids from KPC in the Saltoro Valley comprise albite, microcline, quartz, and biotite as major components, while hornblende and kaolinite comprise minor mineralogy.

The alteration mineral maps (Fig. 5 & 6) show the lithological control over the alteration minerals. Kaolinite has been mapped in Dassu gneiss (Shigar Valley), leucogranite (Raikot Valley), HPU (Hunza Valley), and KPC (Saltoro Valley). According to Fulignati (2020), kaolinite is an alteration product of aluminum silicates (feldspars) and represents an intermediate argillic alteration in acidic conditions (pH 4.5 – 6) at low temperatures (< 200 °C). Alunite (aluminum sulfate) can also be associated with kaolinite at higher temperatures (200 – 300 °C) and lower pH (2 – 4), termed advanced argillic alteration. Alunite has been mapped mostly in intensely altered zones in the Raikot, Shigar, and Hunza valleys. Illite forms due to alteration of K-feldspar and plagioclase above 200 – 300 °C up to 350 °C and represents phyllic to propylitic alteration conditions. Distribution of illite and sericite has been interpreted together as a representation of fine-grained (white) mica and was mapped in gneisses of NPM, Sumayar pluton (Hunza Valley) and contact between Hushe gneiss and KPC (Saltoro Valley). Chlorite and epidote also occur at similar temperatures (200 – 350 °C) through the alteration of mafic (Fe and Mg rich) minerals and are associated with metamorphism (both regional and contact) and hydrothermal alteration (Beaufort et al., 1992). They are mainly mapped in Hushe gneiss, HPU, KMC and lithologies of Kohistan, which are abundant in biotite, amphibole, and pyroxenes.

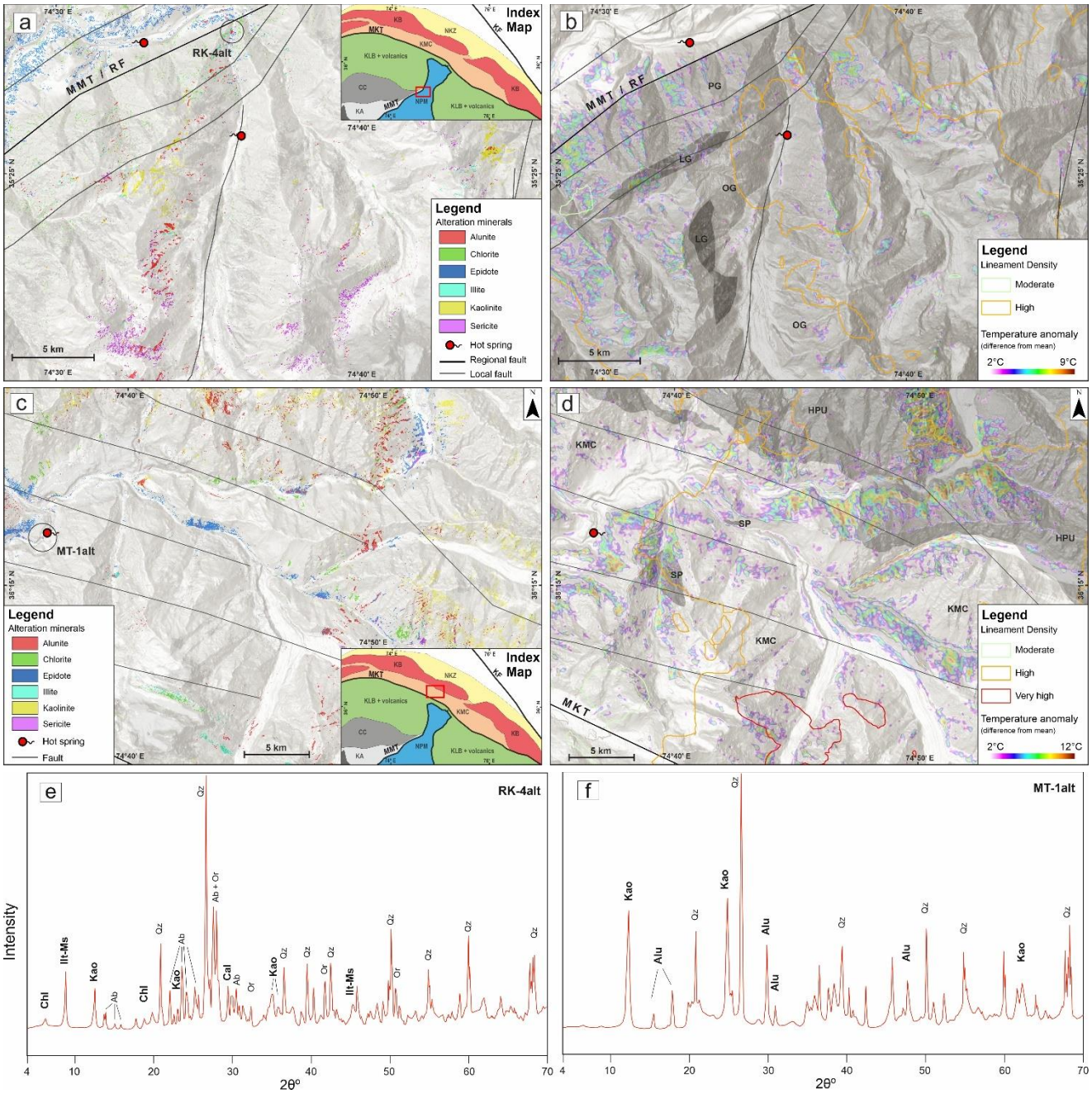

Figure 5: (a) Hydrothermal alteration in the Raikot Valley. RK-4 alt represents the location of the altered sample analyzed using XRD. (b) Distribution of thermal anomalies and lineament density. PG-Paragneiss; OG-Orthogneiss; LG-Leucogranite; RF-Raikot fault. (c) Hydrothermal alteration in the Hunza Valley. MT-1 alt represents the location of the altered sample analyzed using XRD. (d) Distribution of thermal anomalies and lineament density. HPU-Hunza plutonic unit; KMC-Karakoram metamorphic complex; SP-Sumayar pluton. (e & f) XRD patterns of altered samples from the Raikot and Hunza valleys, respectively.

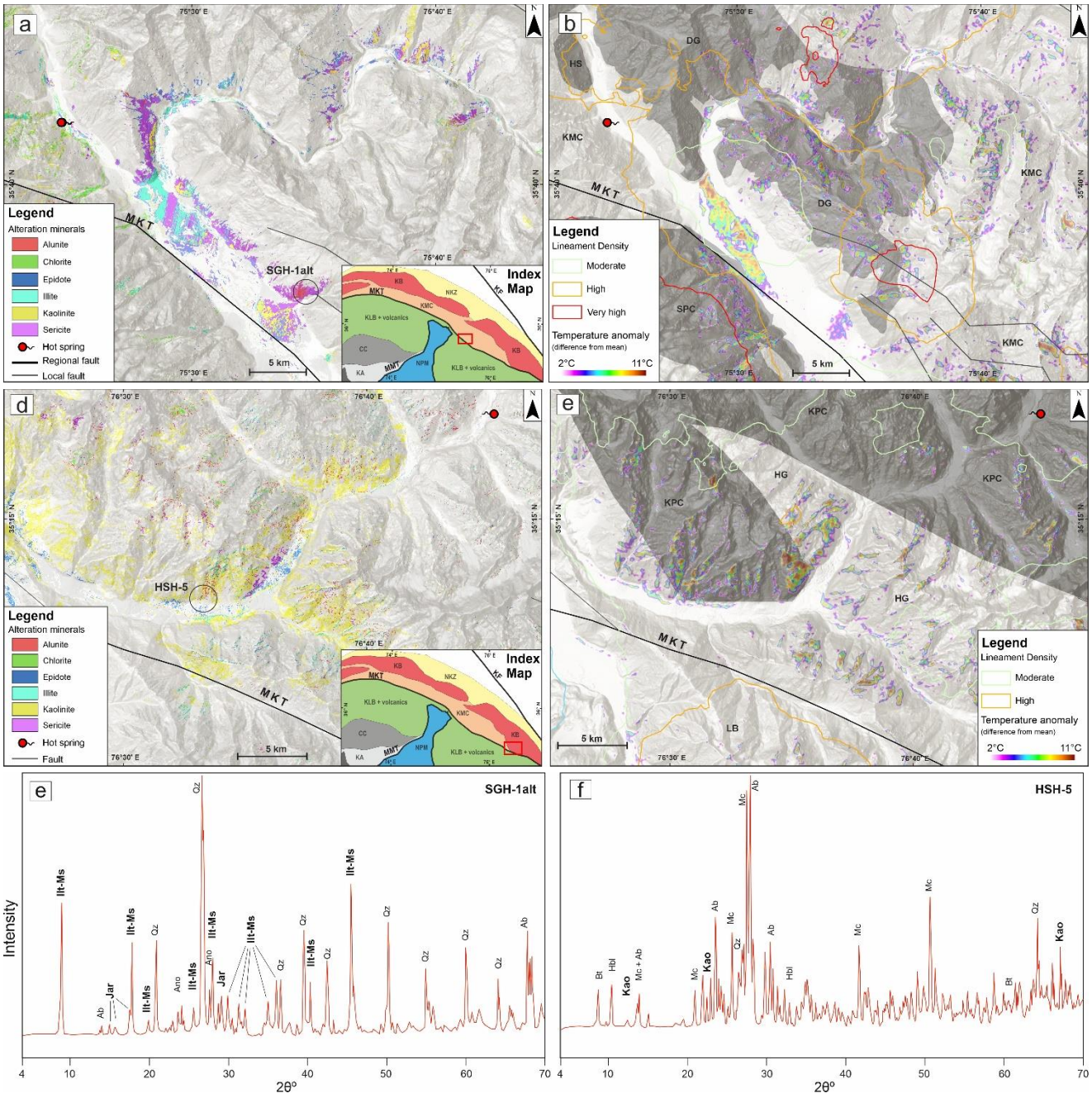

Figure 6: (a) Hydrothermal alteration in the Shigar Valley. SGH-1 alt shows the location of the altered sample analyzed using XRD. (b) Distribution of thermal anomalies and lineament density. DG-Dassu gneiss; KMC-Karakoram metamorphic complex; SPC-Shigar plutonic complex; HS-Hemasil syenite. (c) Hydrothermal alteration in the Saltoro Valley. HSH-5 represents the location of the sample analyzed using XRD. (d) Distribution of thermal anomalies and lineament density. HG-Hushe gneiss; KPC-Kande plutonic complex; LB-Ladakh batholith. (e & f) XRD patterns of altered samples from the Shigar and Saltoro valleys, respectively.

Table 4: Results of semi-quantitative XRD analysis of samples from the study area. (Ab: albite, Alu: alunite, Ano: anorthoclase, Bt: biotite, Cal: calcite, Chl: chlorite, Hbl: hornblende, Ilt: illite, Jar: jarosite, Kao: kaolinite, Mc: microcline, Ms: muscovite, Or: orthoclase, Qz: quartz).

Sample code	Qz	Kfs	Pl	Bt	Amp	Alu	Chl	Ep	Ilt-Ms-Ser	Kao	Cal-Dol	Jar	Tur
AST-8i	+++	++	+++						++				
RK-4i	+++	++	++	++			+		+				
RK-4i alt	+++	++	+++	++			+			+	+		
TTP-3	+++	+	++	+++			+						+
TTP-4	+++	++	++						+				
FM-4	+++	++	++						+				+
KOH-4	+++	+	++	++	+						+		
YK-2	+++		+++	+	++		+				+		
SGH-1	+++			+					++				
SGH-1 alt	+++	+	++						++			+	
SGH-9		++	+++	++				+	+				
KDS-1	+++	+++	+++	+			+		+				
HSH-5	++	+++	+++	++	+					+			
MT-1 alt	+++					++				++			
GL-alt	+++		+++	++									

+++: >25 %, ++: >10 % and +: <5 %

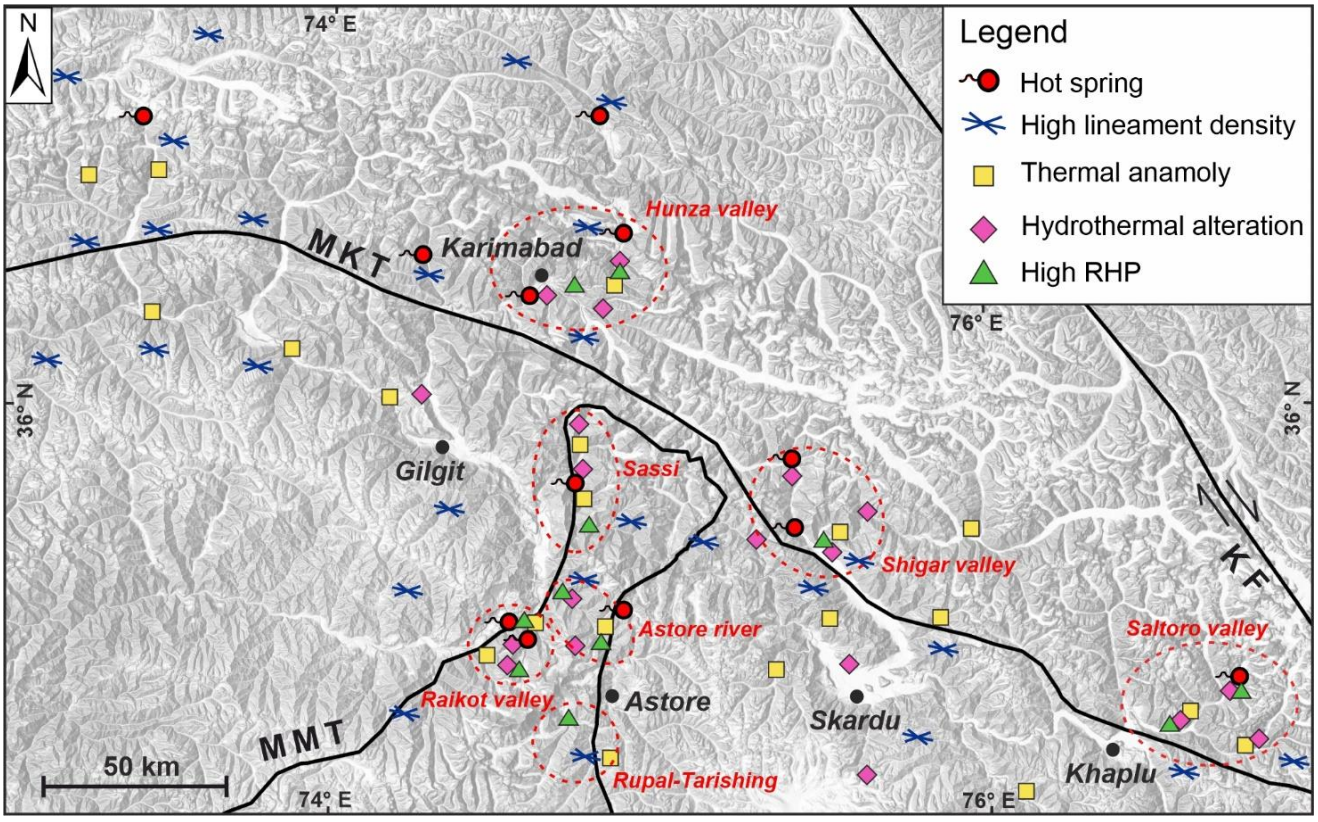

Figure 7: Compilation map showing areas with high radiogenic heat production (after Anees et al., 2023), hydrothermal alteration, thermal anomalies, and high lineament density. Dashed red circles represent areas with high promising geothermal potential.

4.5 Potential geothermal targets

The findings of this study are compiled in a map to identify the promising zones of geothermal potential for further exploration and development (Fig. 7). In the Nanga Parbat Massif, we have identified evidences of active and fossil geothermal activity in the Raikot Valley, Astore River, Rupal-Tarishing, and Sassi. The high radiogenic heat production (RHP) in the NPM suggest presence of hot rocks closer to the surface which is exploited by meteoric water percolating from elevated areas and discharging in the low-lying valleys. The fluid flow is controlled by fault-induced fractures, which could act as hydrothermal reservoirs underlying the topographic lows (close to rivers) and potentially offer high temperatures (> 100°C) at depths of ~2 – 3 km below the surface.

In the central Karakoram, the Hunza and Shigar valleys display indications of geothermal potential. Karakoram batholith and metamorphic complex in Hunza Valley has moderate heat production and numerous intruded dikes and stocks of radiogenic young granites. Along these intrusions, hydrothermal alterations are common in country rocks. The batholith forms a topographic high, has high lineament density, and acts as the recharge zone for hot springs. The imbricate thrusts in the metamorphic complex provide pathways for hydrothermal water, manifested by hot springs at the surface. Ahmed et al. (2001) estimated the subsurface reservoir temperature to be > 150 °C between 2000 to 4000 m below the surface. Hot spring sites in the upper Shigar Valley are in proximity to heat-producing felsic gneiss of the Karakoram metamorphic complex intruded by numerous pegmatitic dikes and a syenitic body. Close to the MKT, the hydrothermal alteration and increased lineament density are more prominent. This metamorphic complex with high RHP could have a higher subsurface temperature.

The Kande pluton of the Karakoram batholith showed the highest RHP values. Surface thermal anomalies, hydrothermal alteration and dense lineaments all point towards warm fractured rock surfaces with thermal imprints. The pluton could be a potential of a hot-dry rock prospect with high enough temperature (> 100°C) at depths of ~2 – 3 km for geothermal exploitation.

5. CONCLUSION

The Himalaya-Karakoram region of north Pakistan, with numerous hot springs, presents promising signs for geothermal energy. However, identifying and exploring geothermal resources in this vast, rugged, and inaccessible terrain is quite challenging. This study used a remote sensing approach to identify regions with high lineament density, surface temperature, and hydrothermal alteration. High lineament density is correlated with intense folding and faulting near major faults and suture zones. Thermal anomalies obtained after removing topographic effects showed some correlation with high lineament density and surface geothermal manifestations, but high uncertainty due to other environmental factors constrained their utility. Alteration minerals mapped in the area identified both previously known and unknown hydrothermal zones. These remote sensing-based results proved helpful in providing base information for field investigation, and the results were confirmed by XRD analysis. Given the results presented here, it is highly recommended to integrate remote sensing for geothermal exploration in an underexplored and topographically challenging area. The remote sensing results, in addition to providing base information for field surveys, can also be extrapolated to remote sites with confidence after field verification. The findings of this study improve the understanding of the region's geothermal regime and identified areas for future detailed geothermal exploration.

AKNOWLEDGMENTS

This project has been funded through a doctoral fellowship by the DAAD (Deutscher Akademischer Austauschdienst) through the German Federal Ministry of Education. Furthermore, the project also recieved funding from the DFG (Deutsche Forschungsgemeinschaft; Project KL 495/32-1) and GAUSS (Georg-August University of Göttingen School of Science) for fieldwork.

REFERENCES

Ahmad, M., Akram, W., Ahmad, N., Tasneem, M. A., Rafiq, M., & Latif, Z. (2002). Assessment of reservoir temperatures of thermal springs of the northern areas of Pakistan by chemical and isotope geothermometry. Geothermics, 31(5), 613–631.

Ahmad, M., Akram, W., Hussain, S. D., Sajjad, M. I., & Zafar, M. S. (2001). Origin and subsurface history of geothermal water of Murtazabad area, Pakistan—Isotopic evidence. Applied Radiation and Isotopes, 55(5), 731–736.

Ahmadi, H., & Pekkan, E. (2021). Fault-based geological lineaments extraction using remote sensing and GIS—a review. Geosciences, 11(5), 183.

Anees, M., Kley, J., Leiss, B., Hindle, D., Wajid, A. A., Wagner, B., Shah, M. M., & Luijendijk, E. (2023). Application of in-situ gamma spectrometry for radiogenic heat production estimation in the Western Himalaya, Kohistan, and Karakoram in northern Pakistan. Geothermal Energy, 11(1), 29.

Arnórsson, S., Bjarnason, J. Ö., Giroud, N., Gunnarsson, I., & Stefánsson, A. (2006). Sampling and analysis of geothermal fluids. Geofluids, 6(3), 203–216.

Awdal, A. H., Braathen, A., Wennberg, O. P., & Sherwani, G. H. (2013). The characteristics of fracture networks in the Shiranish Formation of the Bina Bawi Anticline; comparison with the Taq Taq Field, Zagros, Kurdistan, NE Iraq. Petroleum Geoscience, 19(2), 139–155.

Barbier, E. (2002). Geothermal energy technology and current status: An overview. Renewable and Sustainable Energy Reviews, 6(1), 3–65.

Barbier, M., Leprêtre, R., Callot, J.-P., Gasparrini, M., Daniel, J.-M., Hamon, Y., Lacombe, O., & Floquet, M. (2012). Impact of fracture stratigraphy on the paleo-hydrogeology of the Madison Limestone in two basement-involved folds in the Bighorn basin, (Wyoming, USA). Tectonophysics, 576–577, 116–132.

Beaufort, D., Patrier, P., Meunier, A., & Ottaviani, M. M. (1992). Chemical variations in assemblages including epidote and/or chlorite in the fossil hydrothermal system of Saint Martin (Lesser Antilles). Journal of Volcanology and Geothermal Research, 51(1–2), 95–114.

Butler, R. W. (2019). Tectonic evolution of the Himalayan syntaxes: The view from Nanga Parbat. Geological Society, London, Special Publications, 483(1), 215–254.

Butler, R. W., & Prior, D. J. (1988). Tectonic controls on the uplift of the Nanga Parbat Massif, Pakistan Himalayas. Nature, 333(6170), 247–250.

Butler, R. W., Harris, N. B., & Whittington, A. G. (1997). Interactions between deformation, magmatism and hydrothermal activity during active crustal thickening: A field example from Nanga Parbat, Pakistan Himalayas. Mineralogical Magazine, 61(404), 37–52.

Butler, R. W., Prior, D. J., & Knipe, R. J. (1989). Neotectonics of the Nanga Parbat syntaxis, Pakistan, and crustal stacking in the Northwest Himalayas. Earth and Planetary Science Letters, 94(3–4), 329–343.

Chamberlain, C. P., Koons, P. O., Meltzer, A. S., Park, S. K., Craw, D., Zeitler, P., & Poage, M. A. (2002). Overview of hydrothermal activity associated with active orogenesis and metamorphism: Nanga Parbat, Pakistan Himalaya. American Journal of Science, 302(8), 726–748.

Chamberlain, C. P., Zeitler, P. K., Barnett, D. E., Winslow, D., Poulson, S. R., Leahy, T., & Hammer, J. E. (1995). Active hydrothermal systems during the recent uplift of Nanga Parbat, Pakistan Himalaya. Journal of Geophysical Research: Solid Earth, 100(B1), 439–453.

Coolbaugh, M. F., Kratt, C., Fallacaro, A., Calvin, W. M., & Taranik, J. V. (2007). Detection of geothermal anomalies using advanced spaceborne thermal emission and reflection radiometer (ASTER) thermal infrared images at Bradys Hot Springs, Nevada, USA. Remote Sensing of Environment, 106(3), 350–359.

Craw, D., Chamberlain, C. P., Zeitler, P. K., & Koons, P. O. (1997). Geochemistry of a dry steam geothermal zone formed during rapid uplift of Nanga Parbat, northern Pakistan. Chemical Geology, 142(1–2), 11–22.

Crawford, M. B., & Searle, M. P. (1992). Field relationships and geochemistry of pre-collisional (India-Asia) granitoid magmatism in the central Karakoram, northern Pakistan. Tectonophysics, 206(1–2), 171–192.

Crósta, A. P., De Souza Filho, C. R., Azevedo, F., & Brodie, C. (2003). Targeting key alteration minerals in epithermal deposits in Patagonia, Argentina, using ASTER imagery and principal component analysis. International Journal of Remote Sensing, 24(21), 4233–4240.

Fulignati, P. (2020). Clay minerals in hydrothermal systems. Minerals, 10(10), 919.

Gaetani, M., Angiolini, L., Nicora, A., Sciunnach, D., Le Fort, P., Tanoli, S., & Khan, A. (1996). Reconnaissance geology in Upper Chitral, Baroghil and Karambar districts (northern Karakorum, Pakistan). Geologische Rundschau, 85(4), 683–704.

Gansser, A. (1980). The significance of the Himalayan suture zone. Tectonophysics, 62(1–2), 37–52.

Haselwimmer, C., & Prakash, A. (2013). Thermal Infrared Remote Sensing of Geothermal Systems. In C. Kuenzer & S. Dech (Eds.), Thermal Infrared Remote Sensing (Vol. 17, pp. 453–473). Springer Netherlands.

Hochstein, M. P., & Regenauer-Lieb, K. (1998). Heat generation associated with collision of two plates: The Himalayan geothermal belt. Journal of Volcanology and Geothermal Research, 83(1), 75–92.

Hochstein, M. P., & Zhongke, Y. (1995). The Himalayan Geothermal Belt (Kashmir, Tibet, West Yunnan). In M. Yamano & M. L. Gupta (Eds.), Terrestrial Heat Flow and Geothermal Energy in Asia, Oxford-IBH Publishing Co, New Delhi (pp. 331–386).

Hugman Iii, R. H. H., & Friedman, M. (1979). Effects of texture and composition on mechanical behavior of experimentally deformed carbonate rocks. AAPG Bulletin, 63(9), 1478–1489.

Kana, J. D., Djongyang, N., Danwe Raïdandi, Njandjock Nouck, P., & Abdouramani Dadjé. (2015). A review of geophysical methods for geothermal exploration. Renewable and Sustainable Energy Reviews, 44, 87–95.

Kazmi, A. H., Lawrance, R. D., Dawood, H., Snee, L. W., & Hussain, S. S. (1984). Geology of The Indus Suture Zone In The Mingora-Swat Shangla Area Of Swat, N. Pakistan. Journal of Himalayan Earth Sciences, 17.

Kruse, F. A. (2004). Comparison of ATREM, ACORN, and FLAASH atmospheric corrections using low-altitude AVIRIS data of Boulder, CO. Summaries of 13th JPL Airborne Geoscience Workshop, Jet Propulsion Lab, Pasadena, CA, 1–10.

Madin, I. P., Lawrence, R. D., & Ur-Rehman, S. (1989). The northwestern Nanga Parbat–Haramosh Massif; Evidence for crustal uplift at the northwestern corner of the Indian Craton. In L. L. Malinconico Jr. & R. J. Lillie (Eds.), Tectonics of the western Himalayas (Vol. 232, pp. 169–182). Geological Society of America Special Papers.

Marshak, S., & Mitra, G. (1988). Basic methods of structural geology. New Jersey: Prentice Hall.

Muhammad, S., & Haq, A. (2022). Spatial distribution of radon contamination in hot springs water and its cancer and non-cancer risks in the Hunza-Nagar valley, Pakistan.

Nelson, A. E. (1985). Major tectonic features and structural elements in the northwest part of the Greenville Quadrangle, Georgia (Report 1643; Bulletin). US Geological Survey; USGS Publications Warehouse.

O'leary, D. W., Friedman, J. D., & Pohn, H. A. (1976). Lineament, linear, lineation: Some proposed new standards for old terms. Geological Society of America Bulletin, 87(10), 1463–1469.

Palin, R. M., Searle, M. P., Waters, D. J., Horstwood, M. S. A., & Parrish, R. R. (2012). Combined thermobarometry and geochronology of peraluminous metapelites from the Karakoram metamorphic complex, North Pakistan; New insight into the tectonothermal evolution of the Baltoro and Hunza Valley regions. Journal of Metamorphic Geology, 30(8), 793–820.

Petterson, M. G. (2010). A review of the geology and tectonics of the Kohistan island arc, north Pakistan. Geological Society, London, Special Publications, 338(1), 287–327.

Petterson, M. G., Crawford, M. B., & Windley, B. F. (1993). Petrogenetic implications of neodymium isotope data from the Kohistan batholith, North Pakistan. Journal of the Geological Society, 150(1), 125–129.

Ramakrishnan, D., Bharti, R., Singh, K. D., & Nithya, M. (2013). Thermal inertia mapping and its application in mineral exploration: Results from Mamandur polymetal prospect, India. Geophysical Journal International, 195(1), 357–368.

Schneider, D. A., Edwards, M. A., Kidd, W. S. F., Asif Khan, M., Seeber, L., & Zeitler, P. K. (1999). Tectonics of Nanga Parbat, western Himalaya: Synkinematic plutonism within the doubly vergent shear zones of a crustal-scale pop-up structure. Geology, 27(11), 999–1002.

Searle, M. P., & Khan, M. A. (1996). Geological map of north Pakistan and adjacent areas of northern Ladakh and western Tibet (Western Himalaya, Salt Ranges, Kohistan, Karakoram, Hindu Kush) [Map]. Oxford University.

Searle, M. P., & Tirrul, R. (1991). Structural and thermal evolution of the Karakoram crust. Journal of the Geological Society, 148(1), 65–82.

Searle, M. P., Parrish, R. R., Thow, A. V., Noble, S. R., Phillips, R. J., & Waters, D. J. (2010). Anatomy, age and evolution of a collisional mountain belt: The Baltoro granite batholith and Karakoram Metamorphic Complex, Pakistani Karakoram. Journal of the Geological Society, 167(1), 183–202.

Searle, M. P., Rex, A. J., Tirrul, R., Rex, D. C., Barnicoat, A., & Windley, B. F. (1989). Metamorphic, magmatic, and tectonic evolution of the central Karakoram in the Biafo-Baltoro-Hushe regions of northern Pakistan. In L. L. Malinconico Jr. & R. J. Lillie (Eds.), Tectonics of the western Himalayas (Vol. 232, p. 0). Geological Society of America.

Shuja, T. A. (1986). Geothermal areas in Pakistan. Geothermics, 15(5–6), 719–723.

Singh, A., & Harrison, A. (1985). Standardized principal components. International Journal of Remote Sensing, 6(6), 883–896.

Singh, B. (1993). Geological set up of a part of the Ladakh Granitoid Complex, Ladakh Himalaya. Journal of Himalayan Geology, 4(1), 57–62.

Suzen, M. L., & Toprak, V. (1998). Filtering of satellite images in geological lineament analyses: An application to a fault zone in Central Turkey. International Journal of Remote Sensing, 19(6), 1101–1114.

Tahirkheli, R. K. (1979). Geology of Kohistan and adjoining Eurasian and Indo-Pakistan continents, Pakistan. Geol. Bull. Univ. Peshawar, 11(1), 1–30.

Thannoun, R. G. (2013). Automatic extraction and geospatial analysis of lineaments and their tectonic significance in some areas of Northern Iraq using remote sensing techniques and GIS. International Journal of Enhanced Research in Science Technology & Engineering Bulletin, 2(2), 1–11.

Tong, W., & Zhang, J. (1981). Characteristics of geothermal activities in Xizang plateau and their controlling influence on plateau's tectonic model. Geological and Ecological Studies of the Quinghai-Xizang Plateau, 841–846.

Treloar, P. J., Brodie, K. H., Coward, M. P., Jan, M. Q., Khan, M. A., Knipe, R. J., Rex, D. C., & Williams, M. P. (1990). The evolution of the Kamila shear zone, Kohistan, Pakistan. In M. H. Salisbury & D. M. Fountain (Eds.), Exposed cross-sections of the continental crust (Vol. 317, pp. 175–214). Springer.

Treloar, P. J., Petterson, M. G., Jan, M. Q., & Sullivan, M. A. (1996). A re-evaluation of the stratigraphy and evolution of the Kohistan arc sequence, Pakistan Himalaya: Implications for magmatic and tectonic arc-building processes. Journal of the Geological Society, 153(5), 681–693.

Ulusoy, İ., Labazuy, P., & Aydar, E. (2012). STcorr: An IDL code for image based normalization of lapse rate and illumination effects on nighttime TIR imagery. Computers & Geosciences, 43, 63–72.

van der Meer, F. D., van der Werff, H. M., van Ruitenbeek, F. J., Hecker, C. A., Bakker, W. H., Noomen, M. F., Van Der Meijde, M., Carranza, E. J. M., De Smeth, J. B., & Woldai, T. (2012). Multi-and hyperspectral geologic remote sensing: A review. International Journal of Applied Earth Observation and Geoinformation, 14(1), 112–128.

van der Meer, F., Hecker, C., van Ruitenbeek, F., van der Werff, H., de Wijkerslooth, C., & Wechsler, C. (2014). Geologic remote sensing for geothermal exploration: A review. International Journal of Applied Earth Observation and Geoinformation, 33, 255–269.

Villa, I. M., Lemennicier, Y., & Le Fort, P. (1996). Late Miocene to Early Pliocene tectonometamorphism and cooling in south-central Karakorum and Indus-Tsangpo suture, Chogo Lungma area (NE Pakistan). Tectonophysics, 260(1–3), 201–214.

Wajid, A. A., Anees, M., Alam, S. U., Gorchani, J. K., Shahzad, K., Israr, A., & Shafique, M. (2021). Lineament mapping for a part of the Central Sulaiman Fold–Thrust Belt (SFTB), Pakistan. Arabian Journal of Geosciences, 14(15), 1438.

Watkins, H., Butler, R. W. H., Bond, C. E., & Healy, D. (2015). Influence of structural position on fracture networks in the Torridon Group, Achnashellach fold and thrust belt, NW Scotland. Journal of Structural Geology, 74, 64–80.

Yalcin, M., Kilic Gul, F., Yildiz, A., Polat, N., & Basaran, C. (2020). The mapping of hydrothermal alteration related to the geothermal activities with remote sensing at Akarcay Basin (Afyonkarahisar), using Aster data. Arabian Journal of Geosciences, 13(21), 1166.

Yang, K., Browne, P. R. L., Huntington, J. F., & Walshe, J. L. (2001). Characterising the hydrothermal alteration of the Broadlands–Ohaaki geothermal system, New Zealand, using short-wave infrared spectroscopy. Journal of Volcanology and Geothermal Research, 106(1–2), 53–65.

Yousafzai, A., Eckstein, Y., & Dahl, P. S. (2010). Hydrochemical signatures of deep groundwater circulation in a part of the Himalayan foreland basin. Environmental Earth Sciences, 59, 1079–1098.

Zaigham, N. A., Nayyar, Z. A., & Hisamuddin, N. (2009). Review of geothermal energy resources in Pakistan. Renewable and Sustainable Energy Reviews, 13(1), 223–232.

Zeitler, P. K., Chamberlain, C. P., & Smith, H. A. (1993). Synchronous anatexis, metamorphism, and rapid denudation at Nanga Parbat (Pakistan Himalaya). Geology, 21(4), 347–350.

Zeitler, P. K., Sutter, J. F., Williams, I. S., Zartman, R., & Tahirkheli, R. A. K. (1989). Geochronology and temperature history of the Nanga Parbat–Haramosh massif, Pakistan. In L. L. Malinconico & R. J. Lillie (Eds.), Tectonics of the western Himalayas (Vol. 232, pp. 1–22). Geological Society of America.

Zhang, Y. L., Li, X., Cheng, G. D., Jin, H. J., Yang, D. W., Flerchinger, G. N., Chang, X. L., Wang, X., & Liang, J. (2018). Influences of Topographic Shadows on the Thermal and Hydrological Processes in a Cold Region Mountainous Watershed in Northwest China. Journal of Advances in Modeling Earth Systems, 10(7), 1439–1457.